

ELISA: A Tool for Optimization of Rotor Hover Performance at Low Reynolds Number in the Mars Atmosphere

Witold J. F. Koning
Aerospace Engineer
Science & Technology Corporation
NASA Ames Research Center
Moffett Field, California 94035

B. Natalia Perez Perez
Aerospace Engineer
Science & Technology Corporation
NASA Ames Research Center
Moffett Field, California 94035

Haley V. Cummings
Aerospace Engineer
NASA Ames Research Center
Moffett Field, California 94035

Ethan A. Romander
Aerospace Engineer
NASA Ames Research Center
Moffett Field, California 94035

Wayne Johnson
Aerospace Engineer
NASA Ames Research Center
Moffett Field, California 94035

ABSTRACT

The Evolutionary aLgorithm for Iterative Studies of Aeromechanics (ELISA) was developed in support of the Rotorcraft Optimization for the Advancement of Mars eXploration (ROAMX) project. ELISA was developed to enable aerodynamic rotor hover optimization for low Reynolds number flows in the Mars atmosphere. The first objective of the algorithm allows for unconventional airfoil parameterization and multi-objective airfoil geometry optimization using OVERFLOW. The Pareto-optimal airfoil sets are converted to a set of Pareto-optimal airfoil decks, providing the lowest drag airfoil geometry for each angle of attack, removing the need to arbitrarily select the airfoils to be used in the rotor optimization. The second objective allows for rotor geometry optimization with simultaneous maximization of blade loading and minimization of rotor power using the comprehensive analysis CAMRADII. The result is a Pareto-optimal rotor set, providing the lowest power rotor for each attainable blade loading, and one of the first tools for hover-optimized rotors for high-subsonic low Reynolds number conditions. The airfoil thickness can be modified after the airfoil optimization is complete, allowing for a post-airfoil-optimization adjustment of blade thickness to facilitate conforming to external structural analyses requirements. The relevance of the code is demonstrated with case studies for the ROAMX rotor optimization for Ingenuity-sized single rotors in the Mars atmosphere, a performance study optimizing the chord and twist of Ingenuity's coaxial rotor resulting in the Sample Recovery Helicopters candidate rotor, and high-subsonic low Reynolds number airfoil optimization providing novel insights for higher-efficiency low Reynolds number airfoil geometries and flow physics.

NOTATION

A	rotor disk area, m ²	M_a	section aerodynamic pitch moment, N
c	chord, m	N	number of blades
c_d	section drag coefficient, $D/(0.5\rho_\infty U_\infty^2 c)$	P	rotorcraft power, W
c_l	section lift coefficient, $L/(0.5\rho_\infty U_\infty^2 c)$	r	rotor radial coordinate, m
c_m	section pitch moment coefficient, $M_a/(0.5\rho_\infty U_\infty^2 c^2)$	R	rotor radius, m; range, km
C_p	pressure coefficient, $(p - p_\infty)/(0.5\rho_\infty U_\infty^2)$	Re	chord-based Reynolds number, $\rho_\infty U_\infty c/\mu$
C_P	rotor power coefficient, $P/(\rho_\infty A(\Omega R)^3)$	t	airfoil thickness, m
C_T	rotor thrust coefficient, $T/(\rho_\infty A(\Omega R)^2)$	T	rotor thrust, N; hover time, min.
D	section aerodynamic drag force, N/m	U	velocity, m/s
f	fitness	x	local x coordinate (along chord)
FM	rotor hover figure of merit, $T\sqrt{T/(2\rho_\infty A)}/P$	y	local y coordinate (perpendicular to chord)
L	section aerodynamic lift force, N/m	y^+	dimensionless wall distance
L_{Pareto}	Pareto front length	α	angle of attack, deg
M	Mach number	μ	dynamic viscosity, Ns/m ²
		ρ	density, kg/m ³
		σ	thrust-weighted solidity, $\frac{3N}{\pi R} \int_0^R cr^2 dr$

Ω rotor rotational speed, rad/s

Subscripts

cruise	cruise conditions
d	drag
dd	drag divergence
l	lift
t	thickness
tip	condition at the blade tip
∞	freestream condition
*	reference value

Acronyms

CA	Comprehensive Analysis
ELISA	Evolutionary aLgorithm for Iterative Studies of Aeromechanics
GA	Genetic Algorithm
LE	Leading Edge
MOGA	Multi-Objective Genetic Algorithm
PO-C81	Pareto-optimal C81
ROAMX	Rotor Optimization for the Advancement of Mars eXploration
SRH	Sample Recovery Helicopter
TE	Trailing edge
TRL	Technology Readiness Level
UNS	Unsteady Navier-Stokes

INTRODUCTION

The Mars Helicopter *Ingenuity* made history in April 2021 by being the first aircraft in history to execute powered, controlled flight on another planet [1]. Before *Ingenuity* the high-subsonic low Reynolds number aerodynamics were thought to serve few, if any, practical engineering purposes. *Ingenuity*'s continued success, however, sparked a heightened interest in this aerodynamic regime. While the body of work on rotor aerodynamics at these conditions is still relatively sparse compared to more conventional regimes, it includes notable contributions, including aeromechanical analyses of rotors for Mars conditions at the University of Maryland [2–5], experimental progress on airfoil testing at compressible Reynolds numbers at Tohoku University's Mars Wind Tunnel [6–11], and computational work for airfoils and rotors at Imperial College London [12–14], ONERA and ISAE SUPAERO [15, 16], Politecnico di Torino [17, 18], and various other research groups [19–21].

Previous work investigated rotor performance predictions for *Ingenuity* [22–24], and explored the possible advantages of cambered plate airfoils as direct substitute to the airfoils present on *Ingenuity*'s rotor. Results showed significant improvements in rotor aerodynamic performance [25]. Understanding of low Reynolds number aerodynamics was increased by showing the influence of boundary layer transition to small-scale turbulence on rotor performance for a wide range of environmental conditions [26]. Simulations for an Eppler 387 airfoil showed that the separation, transition, and reattachment of the boundary layer in an

unsteady laminar separation bubble are not governed by small-scale transition up to around $Re = 300,000$ in low freestream turbulence [27]. These findings led future *Ingenuity* predictions to use laminar unsteady Navier-Stokes (UNS) equations to solve for the aerodynamic flowfield at these conditions [24] and led to the insight that the same flow features could then be provoked with unconventional airfoils to potentially improve performance. Optimization of unconventional airfoils was performed and showed that large improvements in aerodynamic sectional performance are possible [28, 29]. Unconventional airfoils were subsequently used in the Mars Science Helicopter concept design to show improvements in rotor performance compared to *Ingenuity* and demonstrated the structural feasibility of very thin rotor blades to be used in Mars rotor applications [5, 30]. These predictions led to the NASA FY21 Space Technology Mission Directorate (STMD) Early Career Initiative (ECI) Project entitled “Rotorcraft Optimization for the Advancement of Mars eXploration” (ROAMX) [31]. The “Evolutionary aLgorithm for Iterative Studies of Aeromechanics” (ELISA) optimization toolset was developed under ROAMX.

The ROAMX rotor goals will first be discussed, and a high-level overview of the ELISA optimization toolset will be presented. Second, use cases for ELISA are presented: the full ROAMX rotor optimization, the planform and twist optimization for the coaxial Sample Recovery Helicopter (SRH) candidate rotor, and airfoil optimization for an advanced airfoil at high-subsonic, low-Reynolds number conditions. Last, concluding remarks and future work will be presented.

ROAMX ROTOR OPTIMIZATION GOALS

The ROAMX project aims to find possible increases in rotor performance for an *Ingenuity*-sized rotor (identical root cutout and radius) by computational optimization and experimental validation of a single rotor in hover, instead of coaxial, to reduce experimental complexity. The sectional airfoil performance is evaluated using OVERFLOW, and the rotor performance is predicted using the comprehensive analysis CAMRADII. Optimizing for rotor hover becomes worthwhile considering the high tip speeds of rotors in the Mars atmosphere and the relatively slow flight speeds of *Ingenuity* (up to 10 m/s [23]), resulting in relatively low advance ratios in forward flight.

Rotor optimization for an *Ingenuity*-sized vehicle in the Mars atmosphere presents several key challenges not yet thoroughly analyzed, compared to studies at higher Reynolds numbers. Optimal airfoils and rotors in the high-subsonic, low Reynolds number regime are still at low Technology Readiness Level (TRL). Furthermore, efficient approaches to model the high-subsonic, low Reynolds number physics using Computational Fluid Dynamics (CFD), especially with regards to turbulence, transition, and strongly separated flows, are not fully defined. Lastly, optimal rotor shapes and

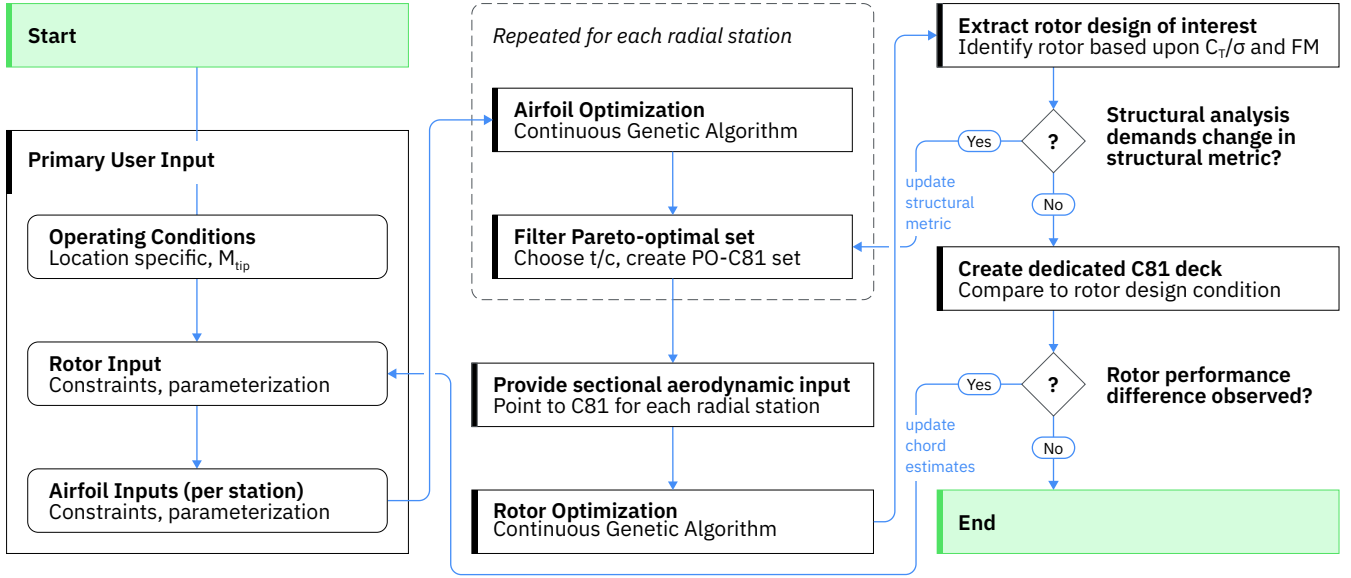


Figure 1. High-level overview of ELISA optimization toolset.

structural analyses of very thin blades at high RPM are complex and can require full 3D structural analyses (compared to using only 2D sectional properties). These challenges, and the lack of a specific mission profile for which to focus the optimization led this project to focus on identifying improvements in possible future rotor performance without predetermined airfoil or rotor design conditions, where possible.

THE ELISA OPTIMIZATION TOOLSET

The high-level workflow of the ELISA optimization toolset is presented in Figure 1. Subsequent sections will describe the algorithm, following the main workflow to provide an account of the key components.

Primary User Input

The first set of user inputs requires the primary flight conditions for the rotor and includes the tip Mach number, M_{tip} , and location-based conditions (atmospheric density, temperature, dynamic viscosity). As the objective of the code is rotor hover optimization, no tradeoffs with cruise speed will be considered and M_{tip} is therefore specified as an input. This avoids optimization up to drag-divergence Mach numbers (and thereby strongly limiting any forward flight speed, M_{cruise}). The tip Mach number is partially estimated by the drag divergence characteristics, M_{dd} , in the aerodynamic regime of interest. In general, it is desired to ensure that $M_{tip} + M_{cruise} \ll M_{dd}$.

User input for the rotor segment includes the rotor radius, rotor root cutout, the radial stations at which airfoil optimization is to be performed, and the corresponding chord estimates at those radial stations. The chord estimates will lead to the Reynolds number estimates for each airfoil,

combined with the operating condition from the previous input block. The rotor chord and twist can both be optimized and are either not parameterized (individual values per radial station), or use a linear, quadratic, or cubic Bézier curve for their parameterization. Radial locations at which negative taper and twist with increased radial location are required can be set. The rotor optimization has dual objectives: maximization of blade loading, C_T/σ , and simultaneous minimization of rotor power, C_P/σ . A minimum C_T/C_P ratio is set to avoid generating designs at very low lift or in stalled conditions, but low-thrust solutions can be kept in the Pareto-optimal rotor selection procedure if so desired.

The airfoil optimization is performed for each radial station in parallel. The airfoil parameterization can be set to `roamx` (dual objectives: maximization of c_l and minimization of c_d) or `roamx3` (`roamx` objectives and maximization of a structural metric or Reynolds number). The structural properties of the airfoil profiles are computed for each iteration and include profile thickness t/c or $(t/c)^2$, or the profile's second moment of area over the chord line. In the current work only t/c is pursued. If `roamx3` optimization is performed, an upper and lower bound of the structural metric can be selected to constrain the optimization to useful values of the structural metric. A desired minimum c_l/c_d threshold is set to avoid optimizing for stalled conditions (which are non-physical in 2D and of limited use), but optionally low c_l values can be included in the Pareto-optimal airfoil selection procedure.

Airfoil Optimization: Geometry Parameterization

The potential of unconventional airfoils (e.g., thin airfoils with sharp leading edges and/or features) was investigated in prior work [25, 28-29]. To more effectively evaluate unconventional airfoil shapes while keeping the number of decision variables to a minimum, the ROAMX

parameterization was developed. Contrary to other approaches, the ROAMX parameterization allows for efficient airfoil parameterization and evaluation at low Reynolds numbers: discontinuities along the airfoil profile can be readily explored, thickness can be fixed if so desired, and the curve order of the camber or thickness segments can be adjusted in order to limit the number of design variables. Figure 2 shows the notation for an example roamx3-0312 airfoil parameterization.

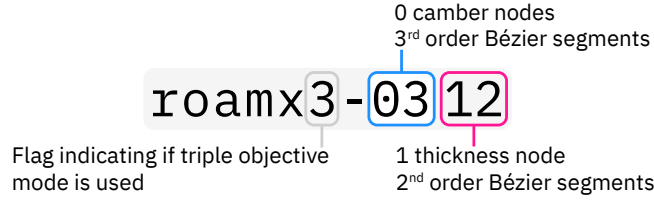


Figure 2. Notation for ROAMX airfoil parameterization.

For both camber and thickness parameterization, the number of ‘nodes’ can be specified, distributed between the leading edge (LE) and the (TE) of the airfoil. These nodes, starting at the LE, are connected by curves as function of chord until the TE is reached. The lines connecting the nodes are represented by Bézier curves which can be chosen to be of first, second, or third order. For each airfoil, the camber, thickness, and a baseline thickness are combined to yield the final airfoil geometry. The baseline thickness is shown in Figure 3, and serves as a minimum thickness constraint (based on manufacturing and/or structural limitations) and is added to the camber distribution.

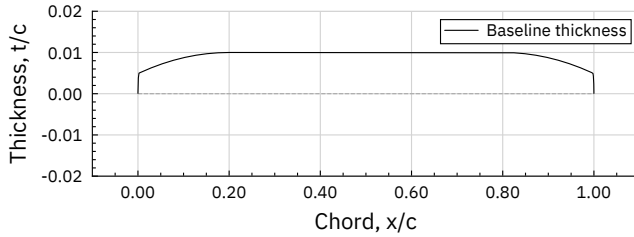


Figure 3. Baseline thickness distribution.

The baseline thickness throughout this work is $t/c = 1\%$. The minimum radii at the LE and TE can also be specified to comply with manufacturing constraints.

An example parameterization for a roamx-0201 airfoil (cambered plate) is shown in Figure 4. The roamx-0201 geometry is specified using 3 decision variables: angle of attack and the two coordinates of the quadratic Bézier control point. Higher order parameterizations include conventional airfoil geometries within the solution space, as shown in Figure 5 for a roamx-0303 parameterization. The roamx-0303 parameterization has 9 decision variables: angle of attack and two pairs of Bézier control points for both thickness and camber.

The primary feature of the ROAMX parameterization scheme allows the user to pick an arbitrary combination of camber and thickness nodes and curve order, allowing for discontinuities along the airfoil profiles, so that

unconventional profiles can be investigated within the solution space. An example of a dragonfly-like airfoil is shown in Figure 6, using a roamx-7201 parameterization.

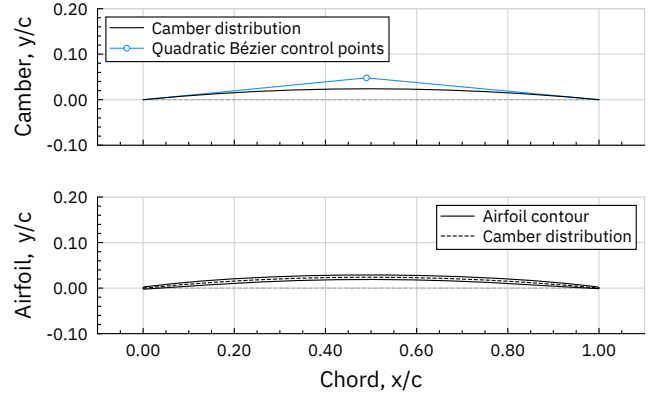


Figure 4. Example roamx-0201 parameterization.

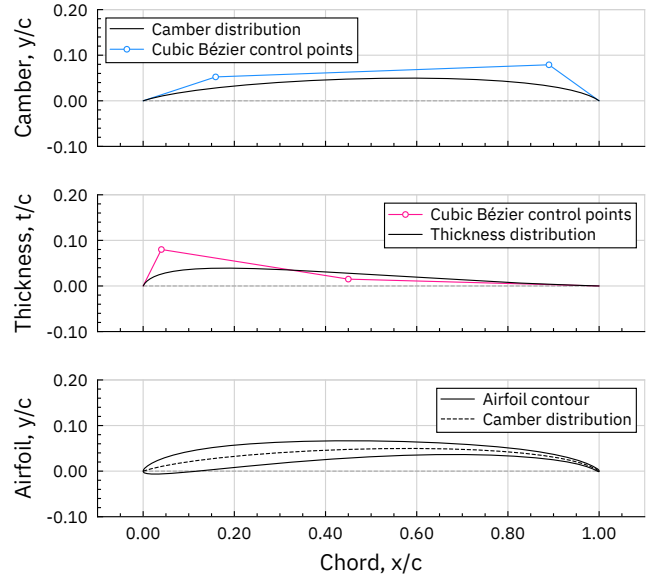


Figure 5. Example roamx-0303 parameterization.

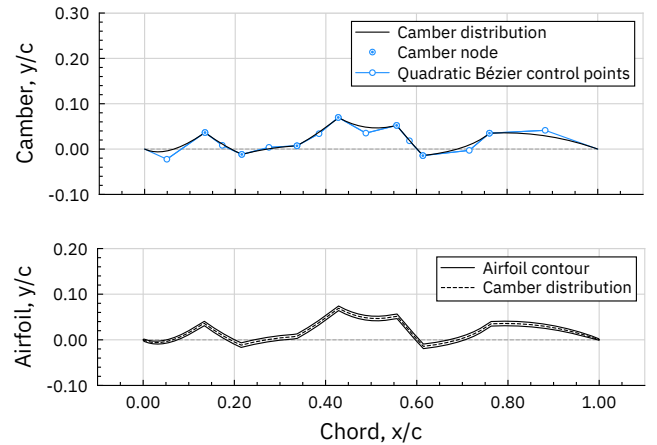


Figure 6. Example roamx-7201 parameterization.

In contrast to the Bézier control points, the nodes are not allowed to cross each other (i.e., for a node n_i the chordwise location is always constrained so that $x_{n_i} < x_{n_{i+1}}$) and the user can set desired (maximum) slopes to constrain the solution space or to avoid difficulties generating grids for strongly concave corners. The ROAMX parameterization scheme automatically updates all node and control point constraints for thickness and camber during each generation depending on the geometry to result in feasible airfoil geometries that can be reasonably manufactured.

Airfoil Optimization: Multi-Objective Airfoil Optimization

The airfoil optimization aims to simultaneously minimize section drag and maximize section lift, resulting in a Pareto-optimal airfoil set. Optionally, the user can specify a third objective which can either be a maximization of a structural metric (the airfoil thickness ratio, t/c , is chosen in the present work) or Reynolds number.

The optimization is performed by a Multi-Objective Genetic Algorithm (MOGA). Compared to gradient-based methods, the advantages of a Genetic Algorithm (GA) here are the ability to readily evaluate non-smooth design spaces (problematic computation of a ‘true mean’ for possibly chaotic and unsteady flows in the compressible low Reynolds number regime complicates gradient-based approaches due to nontrivial finite-differencing in these circumstances). Furthermore, the GA allows for relatively straightforward implementation of multi-objective approaches, allowing computation of Pareto-optimal airfoil and rotor sets as function of airfoil lift, drag, and thickness, and rotor thrust and power, respectively. Finally, the reduced importance of an adequate initial guess close to the global optimum due to the GA’s robustness to a domain with several local minimum solutions (of importance here since optimal airfoil and rotor geometries are simply not known) favors a GA approach.

A GA is an iterative heuristic design space search method that starts with a randomly generated set of ‘individuals’ or ‘chromosomes’ (in this case an airfoil represented by its decision variables, or ‘genes’). The set of chromosomes together form the ‘population’ with each iteration of the MOGA, referred to as a generation. Each generation is evaluated using fitness functions that evaluate the degree to which aerodynamic performance targets are met (and section thickness or Reynolds number targets for roamx3-type optimizations). Selection of nondominated (Pareto-optimal) individuals to modify and advance the solution to a next generation is done using a bin selection method [32], modified here for use for up to 3-objective problems as described in the next section. The genetic operators for the MOGA are passthrough (allowing a fit individual to move to the next generation unmodified), random average crossover (averaging all genes of two randomly sampled nondominated individuals), perturbation mutations (user-specified probability of perturbation per gene), and mutations (user-specified probability of complete mutation per gene). More

detail on the implementation of these operators and fitness functions is found in Refs. [28, 32–34]. For airfoil optimization the MOGA computes a Pareto-optimal set which contains the lowest section drag airfoil geometry for each attainable section lift coefficient. If roamx3-type problems are solved this set can be readily extracted for each thickness (between user selected lower and upper bounds).

In the present work, the algorithm is terminated after ensuring convergence of the Pareto front length. While the heuristic nature of the MOGA is not well suited for finding the exact global solution quickly, the goal here is to explore shapes that are optimal in this space in general and to advance the understanding and TRL of these airfoils and blades, in absence of knowing what optimal geometries look like.

Airfoil Optimization: Bin Selection for Triple-Objective Problems

Evaluation of Pareto-optimality in multiple dimensions readily provides the selection pool for the genetic operators. Less trivial is the selection algorithm in three dimensions. Reference [32] introduces the bin selection algorithm and demonstrates its benefit over classic ‘tournament’ or ‘greedy’ selection procedures. The bin selection algorithm applies to dual objective problems and computes the length between adjacent points along the Pareto front. The selection procedure then first picks the solutions at the endpoints of the Pareto front, and then follows by uniquely sampling the points with the biggest ‘gaps’ in the Pareto front first, until the population size is met. This approach greatly promotes an even distribution along the Pareto front. Furthermore, if an individual is found with a relatively large fitness improvement compared to its neighbors, this procedure equivalently ensures that the fit individual is sampled more frequently due to its distance to its neighbor, propagating the genetic information more frequently as long as the relative advantage (i.e., gap) prevails. This method is used for dual objective problems with 2D Pareto optimal sets. Figure 7 shows an example 3D Pareto front based on fitness values for lift, drag, and thickness.

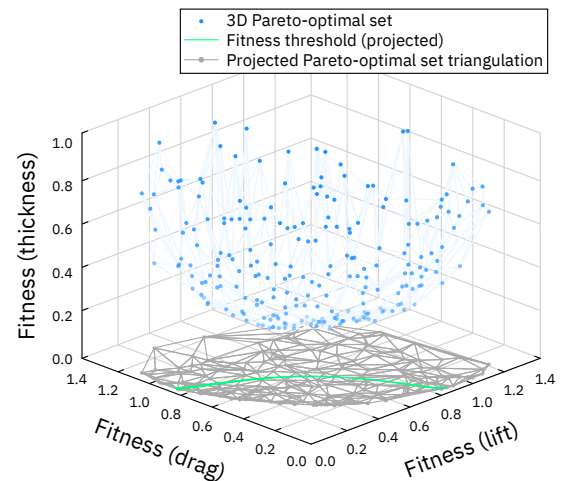


Figure 7. Example 3D Pareto-optimal set.

The fitness values for lift, drag, and thickness are described by

$$f_l = \left(1 - \frac{c_l}{c_l^*}\right)^2 \quad f_d = \left(1 - \frac{c_d}{c_d^*}\right)^2 \quad f_t = \left(1 - \frac{t/c}{t^*}\right)^2,$$

where c_l^* , c_d^* , and t^* are (unattainable) reference values [28]. Due to the nature of Pareto-optimality, one can interpret this front as ‘shell’-like shape, indicated by the Pareto-optimal markers. This therefore allows for computation of the relative separation of the Pareto-optimal cases and its neighbors along the front.

In the ELISA optimization toolset, the bin selection procedure is expanded to allow computation of distance to neighbors in three dimensions. A triangulation is performed on the 3D dataset to create a 3D surface. For clarity, the 2D-projection of the triangulation onto the lift and drag plane is shown in Figure 8.

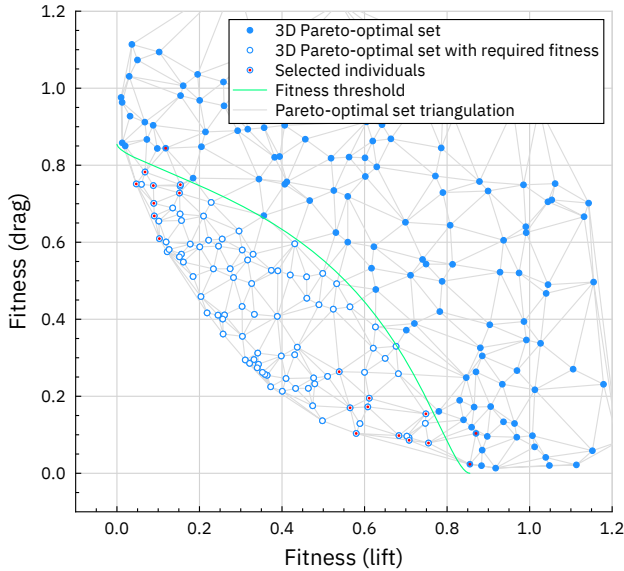


Figure 8. Selection procedure in 3D projected onto the 2D lift and drag plane.

The Pareto-optimal set is reduced to triangles which have at least one of their vertices within the aerodynamic performance threshold (c_l/c_d ratio) and within the lower and upper thickness thresholds. The dataset is now used to compute the area of the 3D triangles. Ordering the triangles by area (large to small) and listing unique nodes allows for the selection of individuals in three-objective space until the population size is met.

Airfoil Optimization: Function Evaluation in OVERFLOW

All airfoil performance function evaluations are performed using 2D Computational Fluid Dynamics (CFD) with structured grids and solved using the implicit, compressible Navier-Stokes solver OVERFLOW 2.3d [35, 36]. Inviscid fluxes are computed using the HLLE++ flux schemes with a 5th-order WENOM upwind reconstruction approach for high

spatial accuracy with low numerical dissipation [37]. Viscous fluxes are computed using 2nd-order central differencing, as are grid metric terms. Time advance uses a 2nd-order backward differencing scheme, with a dual time-stepping approach as described in Refs. [38, 39].

The user can provide the inputs for the airfoil optimization to provide full flexibility to adjust the simulations for the aerodynamic regime of interest. All analyses presented in this work are performed using laminar Unsteady Navier-Stokes (UNS) equations and no turbulence model is employed (as discussed in the following paragraphs). This approach attempts to resolve the flow down to the grid resolution, leaving scales below the grid level (in time or space) unevaluated. Simulations in the present work are set up using a set of coarse timesteps at first to remove the initial transients before starting the time-accurate runs. During post processing, the transients of the time-accurate part of the simulations are evaluated to remove them from the computation of the mean and compute the corresponding confidence intervals, according to Ref. [40].

The location of the LE, nodes, and TE is provided to the grid generation script which automatically refines the chordwise spacing around discontinuities in the grid. The basic grid generation of the airfoils is described in [24, 27], but the maximum chordwise and off body separation was set at 1% c to reduce the grid size and computation time. The dimensionless wall distance is kept below $y^+ = 1$ for all cases. Grid dimensions vary between different analyses presented in this work, but the grid dimensions are on the order of 1000 chordwise and 250 normal grid points.

The hypothesis motivating the numerical approach taken herein is that the smaller scales, while existing, do not contribute meaningfully to the mean forces on the airfoils in the compressible, low Reynolds number regime. This was substantiated by previous work showing satisfactory correlation up to relatively high Reynolds numbers ($Re < 300,000$) for Eppler 387 airfoil performance using laminar UNS at low Reynolds numbers ($60,000 \leq Re \leq 460,000$) to experimental data [27]. The study showed that mean behavior of unsteady Laminar Separation Bubbles (LSB) can be captured accurately using laminar UNS and transition to turbulence was governed by a separated shear layer instability resulting in the shedding of large-scale coherent vortices, resulting in reattachment of the mean flow only. Similar shear layer instabilities are observed in the sectional simulations for the Ingenuity rotor performance model [23, 24] alluding to similar mechanisms at play and the relative importance of large-scale coherent motion, when compared to small-scale turbulence.

The airfoil function evaluation is the constraining element of the ELISA workflow. The airfoil optimization code automatically distributes each chromosome to a dedicated node on the Pleiades Supercomputer at NASA Ames Research Center to compute the whole generational fitness in

parallel to efficiently advance the solutions. For the examples provided in this work, the average solution advance required approximately 45 minutes of wall time per generation and the majority of the Pareto-fronts are well-defined after around 50 to 100 generations.

Pareto-optimal C81 Deck Filtering

“C81 decks” are a specific format of text files of airfoil lift, drag, and moment coefficients, as a function of angle of attack and Mach number (C81 was an early rotorcraft comprehensive analysis program, for which the format was defined). Once airfoil optimization is completed, the Pareto-optimal sets are filtered to generate the Pareto-optimal C81 (PO-C81) decks. If a roamlx3-type optimization is pursued, the 3D Pareto-optimal set (function of c_l , c_d , t/c) is first used to extract a 2D Pareto optimal set (function of c_l , c_d) by evaluating Pareto-optimality subjected to the desired thickness constraint. The 2D Pareto-optimal airfoil set is now arranged as section lift-to-drag ratio versus angle of attack (a decision variable for all airfoil optimizations), as shown in Figure 9.

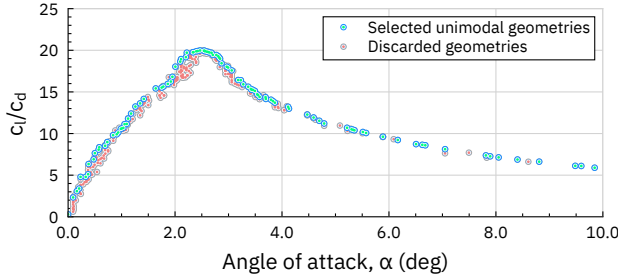


Figure 9. Lift-to-drag ratio filtering of the Pareto-optimal airfoil set.

Next, lower efficiency individuals are discarded by enforcing a strict unimodal (i.e., having only a single highest value) lift-to-drag ratio distribution with angle of attack. Any duplicate angles of attack (down to 2 decimal places) are removed here to avoid ambiguity since angle of attack is used to trace back the airfoil geometries in the rotor optimization phase. The reduced Pareto-optimal set is now ordered as section lift versus angle of attack, as shown in Figure 10.

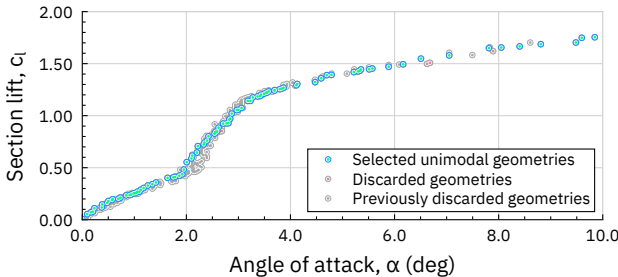


Figure 10. Lift-filtering of the reduced Pareto-optimal airfoil set.

The filter now discards lower lift individuals by enforcing a strict unimodal section lift distribution with angle of attack. The final Pareto-optimal set is now shown in Figure 11.

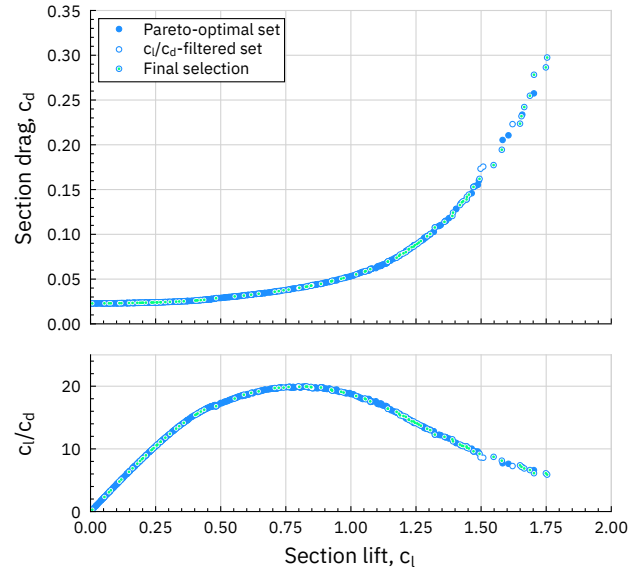


Figure 11. Final filtering of Pareto-optimal airfoil set.

For angles of attack outside of the optimization range, experimental section data for a NACA 0012 profile is automatically added to the set to facilitate the rotor optimization stability. The selection of the Pareto-optimal airfoil set is now finally reduced if the set contains more than the allowable 99 angle of attack entries in a C81 deck. Reduction is implemented by eliminating individuals that are closest to their nearest neighbors in terms of angle of attack.

As the filtered Pareto-optimal set now has a unimodal section lift with respect to angle of attack while keeping the most efficient geometries, the set can now be formatted into proper PO-C81 decks for each radial station. CAMRADII will query the C81 table for performance based on input Mach and angle of attack. Afterwards it will retrieve the section airfoil coefficients for that particular condition – resulting in geometry for the lowest possible drag corresponding to the lift of that entry.

The airfoil geometry is now tied to the angle of attack as CAMRADII, based on lifting line theory, has no particular notion of airfoil geometry.

Rotor Optimization

The rotor optimization is performed using a MOGA, mirroring the approach taken in airfoil optimization. The objectives are twofold: to concurrently minimize rotor power (C_P/σ) and maximize blade loading (C_T/σ), ultimately yielding a Pareto-optimal rotor set. The Pareto-optimal set represents the lowest power rotors across all achievable blade loadings.

Rotor Optimization: Geometry Parameterization

The rotor parameterization closely mirrors the ROAMX airfoil optimization and is designed to parameterize both the twist and planform of the rotor. The same genetic operators

are used to modify each generation. The user can specify ‘no parameterization’ (i.e., each chord and twist value is allowed to individually vary) or a linear, quadratic, or cubic Bézier curves may be used to represent the twist and chord. Figure 12 shows an example twist and chord parameterization using cubic Bézier curves.

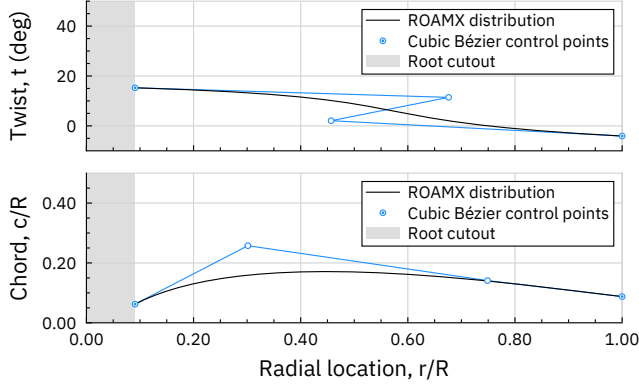


Figure 12. Example ROAMX rotor parameterization, using cubic Bézier curves for twist and chord.

The user can set limits to the chord and twist slopes in the outboard region to help converge to realistic rotor geometries. Furthermore, the user can choose to optimize rotor planform while fixing the thrust-weighted solidity numerically. The root and tip node radial locations are fixed, but the chord and twist values are free (in contrast to the airfoil parameterization where the LE and TE points are fixed). These constraints result in the rotor parameterization in Figure 12 having 12 decision variables (two pairs of coordinates for the cubic Bézier curves, 2 root values, and 2 tip values). The collective is fixed during the optimization, being redundant with twist.

Rotor Optimization: Function Evaluation in CAMRADII

All rotor performance function evaluations are performed using the Comprehensive Analyses (CA) code CAMRADII [41]. The CA model is set up to use the generated PO-C81 tables and predict the corresponding rotor performance. The CAMRADII aerodynamic model for the rotor blade is based on lifting-line theory, using steady two-dimensional airfoil characteristics, a vortex wake model, and additional models for unsteady flow (attached flow and dynamic stall) and yawed/swept flow. Effects of compressibility (Mach numbers) and viscosity (Reynolds number, stall, and drag) enter through airfoil table data: lift, drag, and moment coefficients of two-dimensional sections as function of angle of attack and Mach number, for the appropriate chord and atmosphere (density, temperature) to have correct Reynolds number variation with Mach number.

Rotor Optimization: Dedicated Airfoil Decks

The rotor optimization results in a Pareto-optimal rotor set from which rotor geometries can be extracted for further analysis. As the Reynolds number in the PO-C81 decks

(based on the initial chord estimate from the user) can be different from the actual Reynolds number (based on the chord of the optimized rotor planform), there is the possibility for a mismatch in performance between the optimized rotor performance and the actual rotor performance. Furthermore, the angle of attack distribution in the CAMRADII case is used to trace back the airfoil geometries further allowing for discrepancies between the optimization output and the actual rotor performance. This is because CAMRADII will interpolate angles of attack while the PO-C81 decks technically represent discrete airfoils at specific angles of attack.

To verify the optimized rotor performance, a full set of C81 decks for the acquired airfoil and rotor geometries must be generated, to validate that the performance curves include the rotor design blade loading values. As the rotor blade shape is roughly known beforehand (for a particular solidity at least), the requirement to re-iterate the primary ELISA loop was not required for the use cases presented in this work.

ROAMX ROTOR HOVER OPTIMIZATION

The first use case for the ELISA optimization toolset is the full rotor hover optimization for the ROAMX project [31]. The ROAMX project aims to investigate possible rotor performance improvements for the same rotor radius (and root-cutout) as Ingenuity. A single rotor (instead of coaxial rotor setup) was pursued to facilitate experimental validation in the second phase of the project. The ROAMX rotor optimization is performed for a 6-bladed single rotor with a thrust-weighted solidity of $\sigma = 0.25$.

The operating conditions are chosen to be Ingenuity’s design operating conditions, with a density of $\rho = 0.017 \text{ kg/m}^3$, commonly referred to as ‘Mars Condition 2’ [23]. The airfoil optimization is performed at $r/R = 0.0908, 0.25, 0.50, 0.75, 0.90$, and 1.00 . The inboard two stations were chosen to have roamx3-type optimizations (with variable thickness), and the outboard stations used a total baseline thickness of $t/c = 1\%$. The thin outboard sections allowed for the tip Mach number to be set at $M_{tip} = 0.80$, while still allowing for 30 m/s forward flight speeds, based on early studies investigating drag divergence behavior for these profiles. Very thin, outboard sections similar to this thickness were shown to be structurally feasible in the Mars Science Helicopter concept design [5, 30].

Airfoil Optimization

Figure 13 shows the Pareto-optimal airfoil set for $r/R = 1.00$ (blade tip) conditions, compared to the clf5605 airfoil (used outboard of $r/R = 0.50$ on Ingenuity’s rotor [22]), evaluated at the same conditions. Figure 14 shows the Pareto-optimal airfoil set for $r/R = 0.75$ conditions compared to the clf5605 airfoil. Both airfoils are parameterized using roamx-0201 parameterization (quadratic camber variation).

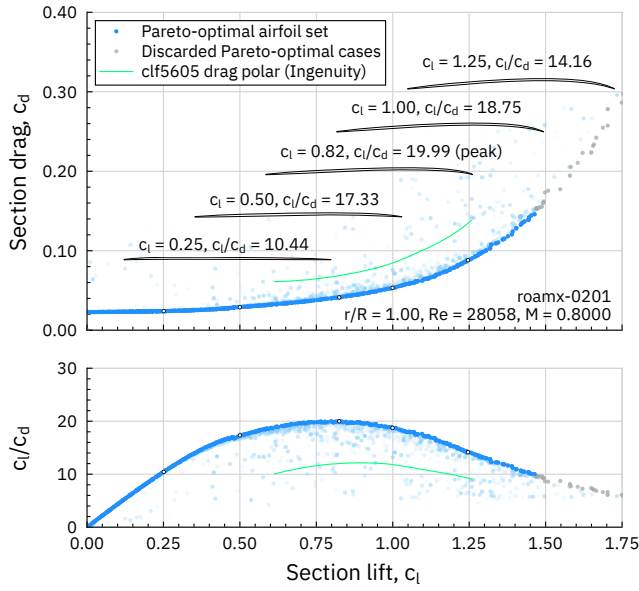


Figure 13. ROAMX airfoil optimization at $r/R = 1.00$ (dual-objective mode).

The largest airfoil performance improvements are possible at the tip conditions, as the lower thickness and sharp LE combine to delay the critical Mach number and improve low Reynolds number airfoil performance. The minimum lift-to-drag ratio requirement for both sets was set to $c_l/c_d \geq 10$, but the low lift individuals were kept in the Pareto-optimal selection if required in the rotor optimization later.

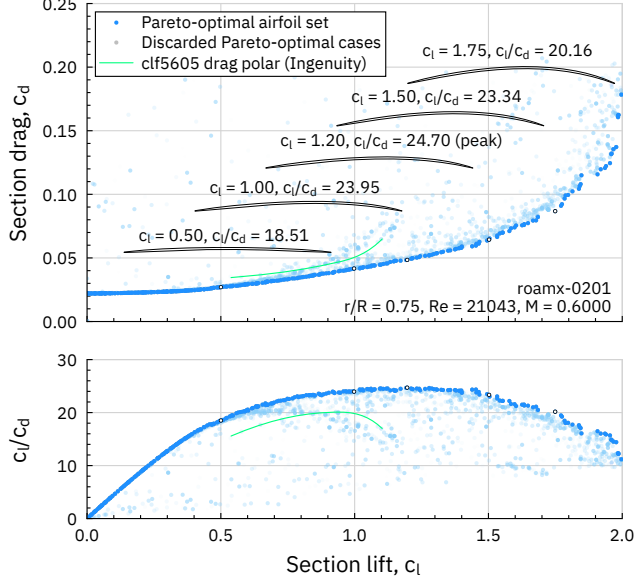


Figure 14. ROAMX airfoil optimization at $r/R = 0.75$ (dual objective mode).

The peak c_l/c_d for the airfoil optimizations at the tip are compared in Table 1. Comparison of airfoil performance for $r/R = 1.00$ ($Re = 28,058$, $M = 0.80$) and the maximum relative change, compared to the clf5605 profile is around 65%. The relative improvements at $r/R = 0.75$ are lower, but still substantial. The peak c_l/c_d for the airfoil optimizations at

$r/R = 0.75$ are compared in Table 2 and the maximum relative change, compared to the clf5605 profile is around 23%.

Table 1. Comparison of airfoil performance for $r/R = 1.00$ ($Re = 28,058$, $M = 0.80$)

Airfoil	c_l/c_d (peak)	Relative change, %	c_l/c_d ($c_l = 0.91^a$)	Relative change, %
clf5605	12.15	—	12.15	—
roamx-0201	19.99	65%	19.58	61%

^a Section lift coefficient for clf5605 peak c_l/c_d at this condition.

Table 2. Comparison of airfoil performance for $r/R = 0.75$ ($Re = 21,043$, $M = 0.60$)

Airfoil	c_l/c_d (peak)	Relative change, %	c_l/c_d ($c_l = 0.91^b$)	Relative change, %
clf5605	20.06	—	20.06	—
roamx-0201	24.70	23%	23.82	19%

^b Section lift coefficient for clf5605 peak c_l/c_d at this condition.

The inboard sections at $r/R = 0.0908$ and 0.25 were optimized using roamx3-type parameterization. This parameterization allowed the Pareto-optimal airfoil sets (as function of lift and drag) to be readily re-evaluated based on structural requirements (here thickness, t/c) as informed by the external structural analysis of the optimized blade [4] after the airfoil and rotor optimization were performed.

Figure 15 shows the airfoil optimization using triple-objective mode, highlighting the Pareto-optimal airfoil set for a $t/c \geq 10\%$ requirement.

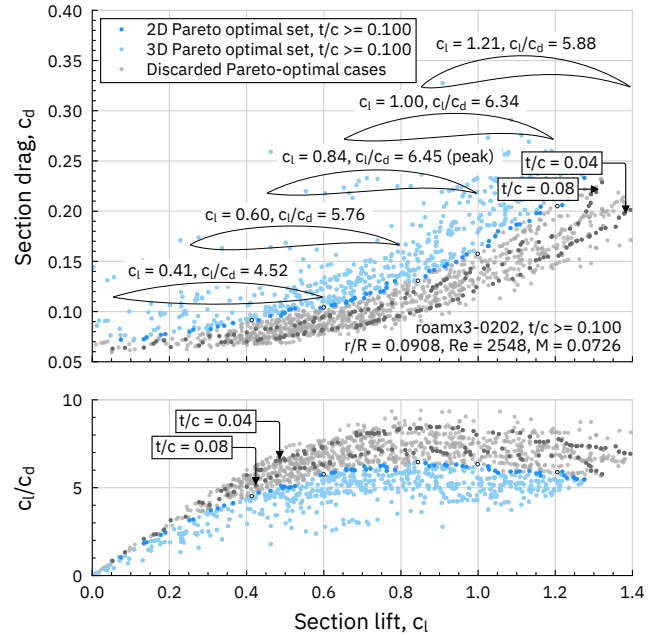


Figure 15. ROAMX airfoil optimization at $r/R = 0.09$ (triple objective mode), 2D Pareto front for $t/c > 0.10$.

The minimum lift-to-drag ratio requirement for the sets was $c_l/c_d = 5$, but the low lift individuals were kept. Additional Pareto-optimal sets for $t/c = 4\%$ and 8% are indicated to illustrate the nature of the 3D Pareto-optimal airfoil set.

To present the convergence of the airfoil optimization, the peak lift-to-drag ratio at $r/R = 0.75$ as function of generation, as shown in Figure 14, is presented in Figure 16. Figure 16 can, however, present a misleading picture as only singular optimized values are shown, versus a representation of the state of the whole Pareto front. In absence of knowing the true final value of the optimization problem, one can plot the length of the Pareto front to get an impression of the convergence instead. Figure 17 shows the normalized Pareto front length during the optimization for $c_l/c_d \geq 10$.

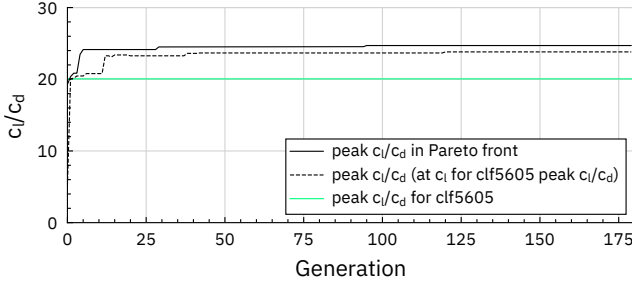


Figure 16. Convergence of ROAMX airfoil optimization at $r/R = 0.75$.

Rotor Optimization

The rotor optimization was evaluated for a fixed thrust-weighted solidity of $\sigma = 0.25$, for a 6-bladed single rotor. The planform and twist distributions were both parameterized using cubic Bézier curves.

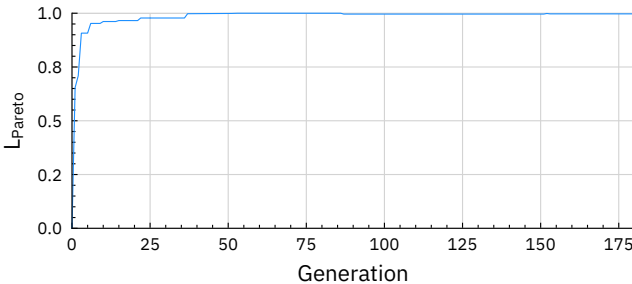


Figure 17. Pareto-front length for ROAMX airfoil optimization at $r/R = 0.75$.

The resulting Pareto-optimal rotor set attempts to simultaneously minimize rotor power, while maximizing blade loading and is presented in Figure 18. Ingenuity performance predictions are presented, modeled as a single 4-bladed rotor in CAMRADII (coaxial benefits are removed to present a fairer comparison) at $M_{tip} = 0.80$.

The Ingenuity design thrust coefficient range is presented as well to identify the primary region of interest. Expressing the dataset as Figure of Merit versus blade loading highlights the attained differences in rotor efficiencies, as shown in Figure 19.

Three design blade loading targets (at $C_T/\sigma = 0.115$, 0.150 , and 0.175) are highlighted in the Pareto optimal set. By extracting the angle of attack over the blade from the CAMRADII cases, the airfoil geometries were obtained for each radial station and each design blade loading. For those rotor geometries dedicated airfoil decks are generated which are used to validate that the design conditions were met, as shown by the dotted lines.

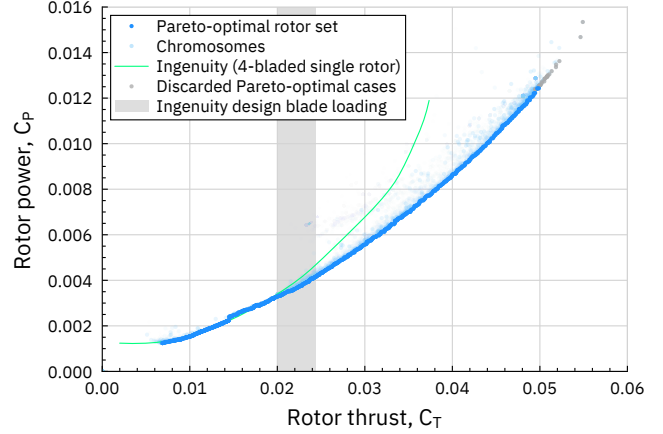


Figure 18. Pareto-optimal rotor set for the ROAMX rotor.

Table 3 shows an overview of the Figure of Merit changes at the design blade loading conditions, compared to Ingenuity's performance (modeled as a single 4-bladed rotor). The highest blade loading design ($C_T/\sigma = 0.175$) was ultimately selected for further investigation in the ROAMX project. The rotor corresponding to this design point will now be called 'the ROAMX rotor'.

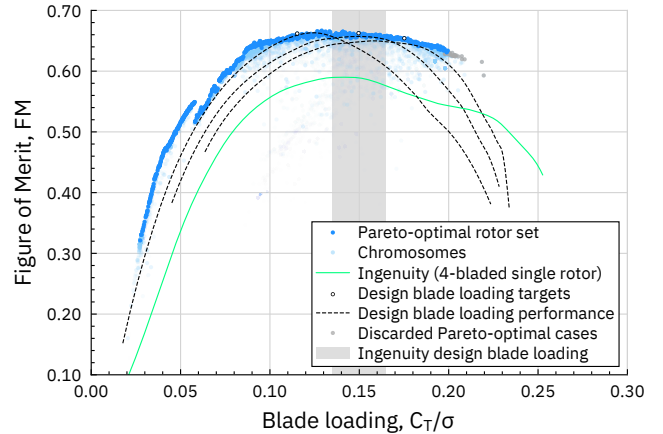


Figure 19. Pareto-optimal rotor set for the ROAMX rotor, including thrust sweeps for 3 design points of interest.

Since the optimization results in single design points, verifying that the rotor is not 'too optimized' and still has a useful thrust margin beyond its design condition is a valuable exercise. As rotor stall is hard to predict accurately, 'thrust margin' is interpreted here as a possible 50% increase in blade loading without reduction of the Figure of Merit. The rotor

hover efficiency for the $C_T/\sigma = 0.175$ rotor design is then $FM = 0.64$ for an effective design blade loading of $C_T/\sigma = 0.125$.

Figure 20 shows the airfoils for the $C_T/\sigma = 0.175$ ROAMX rotor and compares them in the outboard region to the Ingenuity clf5605 profiles.

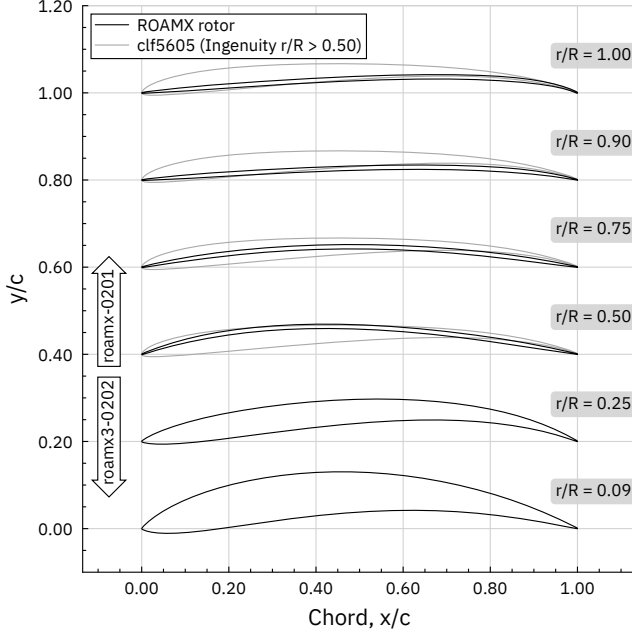


Figure 20. ROAMX rotor ($C_T/\sigma = 0.175$) airfoils compared to Ingenuity outboard.

Figure 21 shows the optimized rotor twist and chord distributions for the ROAMX rotor at $C_T/\sigma = 0.175$. The twist and chord distributions for Ingenuity are plotted for reference, as are the cubic Bézier control points for this optimization.

Table 3. Comparison of ROAMX Rotors to Ingenuity

Rotor geometry	Figure of Merit, FM	Relative Change, % ^c
Ingenuity (4-bladed single rotor, $C_T/\sigma = 0.115$)	0.56	--
ROAMX $C_T/\sigma = 0.115$	0.66	19%
ROAMX $C_T/\sigma = 0.150$	0.66	12%
ROAMX $C_T/\sigma = 0.175$	0.65	15%

^c For equal blade loading.

Full rotating blade structural analysis and design of the carbon-fiber ply layup of the ROAMX blade has been performed in Ref. [4] as shown in Figure 22. The analysis shows that the blade is safe for all testing conditions with a safety factor of two (up to $M_{tip} = 0.95$). The pitch axis was moved to 40% of the chord to significantly reduce blade root loads and 3D stresses.

Despite the low blade thickness and the risk of significant deformation under load, no adjustments of the blade twist were performed to attain predicted performance with a flexible blade analysis. Aerodynamic loads are low (around 1% of the inertial loads), so that the inertial forces are the primary source of stresses in the blade in hover. This warrants decoupling of the aerodynamic and structural analyses as performed in this study to a degree. Despite these points, manufacturing such a blade remains a limitation of the study and warrants further analysis.

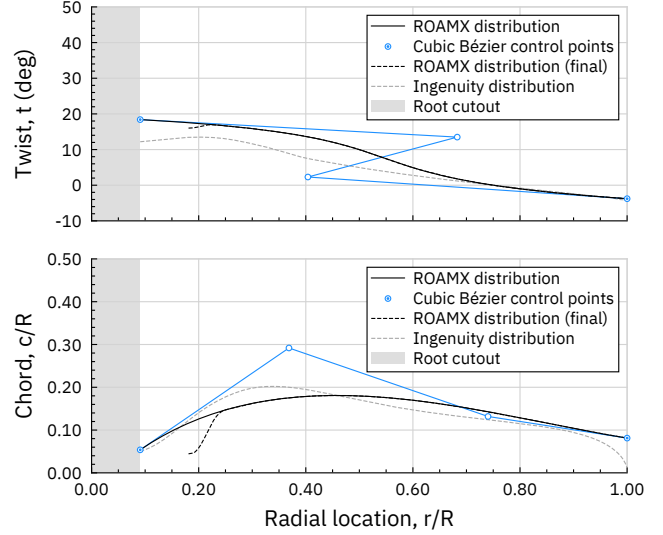


Figure 21. ROAMX rotor planform and twist, compared to Ingenuity.

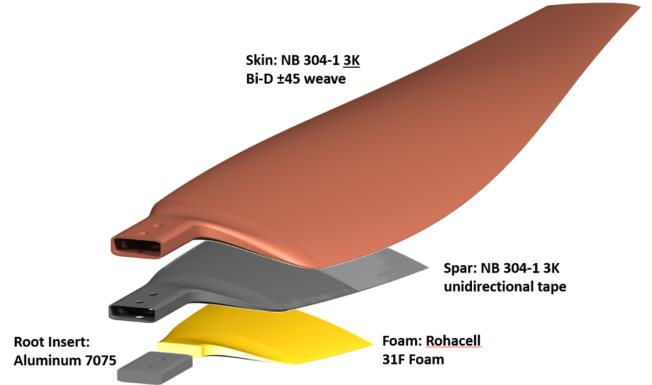


Figure 22. Materials and internal structure of the ROAMX blade, from [4].

The blade has been manufactured, as shown in Figure 23. To accommodate the diameter of the ROAMX hub, the rotor radius was scaled up to $R = 720$ mm, and the root cutout was increased to allow for a larger motor for testing during the ROAMX project. The adjusted root geometry is labeled in Figure 21 as ‘final’.

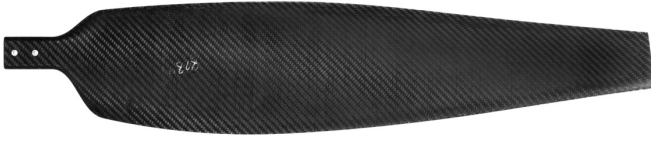


Figure 23. Manufactured ROAMX blade.

Improvements in rotor performance can trickle down into the vehicle design. An increase in Figure of Merit can, for example, reduce the required power, and hence require smaller motors, batteries, resulting in less required thrust, etc. For an Ingenuity-sized vehicle the impact of the ROAMX rotor on vehicle performance is computed and shown in Figure 24, and compared to early airfoil optimization results [28, 30] and Ingenuity's rotor performance model [23, 24] at $M_{tip} = 0.80$.

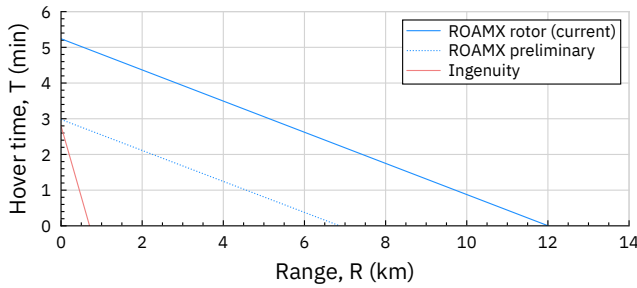


Figure 24. Hover time versus range estimates for an Ingenuity-sized vehicle with various rotors.

Blade Thickness Study

To investigate the influence of the blade thickness on ROAMX rotor performance improvements, a study was performed with triple-objective airfoil optimizations (roamx3-0202 parameterization) for $r/R = 0.0908, 0.25, 0.50, 0.75$ and 1.00 . Rotor optimization was subsequently performed for 2 different blade thickness distributions: minimum $t/c = 5\%$ throughout (Case 2), and linear thickness reduction to $t/c = 1\%$ from $r/R = 0.25$ outboard (Case 1). Expressing the dataset as Figure of Merit versus blade loading highlights the attained differences in rotor efficiencies, as shown Figure 25.

The Pareto-optimal rotor sets show the clear influence of the thickness on attainable rotor figure of merit values. However, Figure 25 also shows that even at a constant $t/c = 5\%$ outboard (Case 2), improvements are still achievable with different rotor geometry and airfoils.

The rotor geometry for $C_T/\sigma = 0.175$ is extracted for the Case 2 thickness profile. Figure 26 shows the airfoils for the roamx3-0202 parameterization and the Case 2 thickness profile (as shown in Figure 25). The ROAMX rotor airfoil profiles in Figure 20 are shown for comparison.

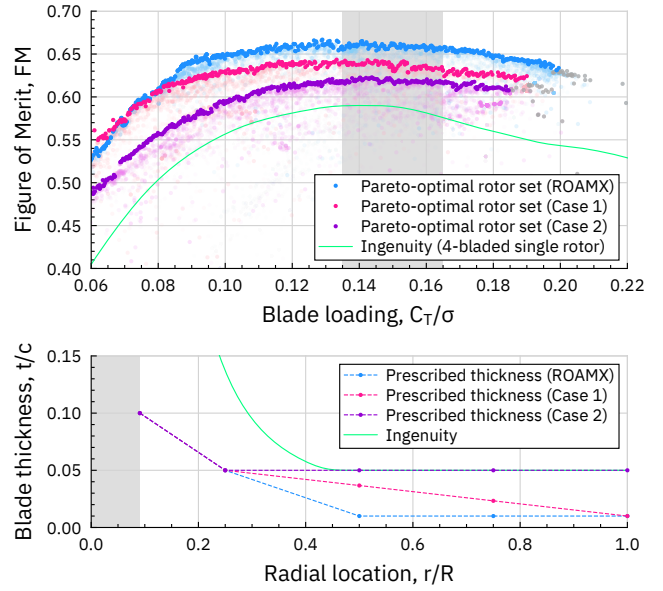


Figure 25. The influence of blade thickness profiles on Pareto-optimal rotor sets.

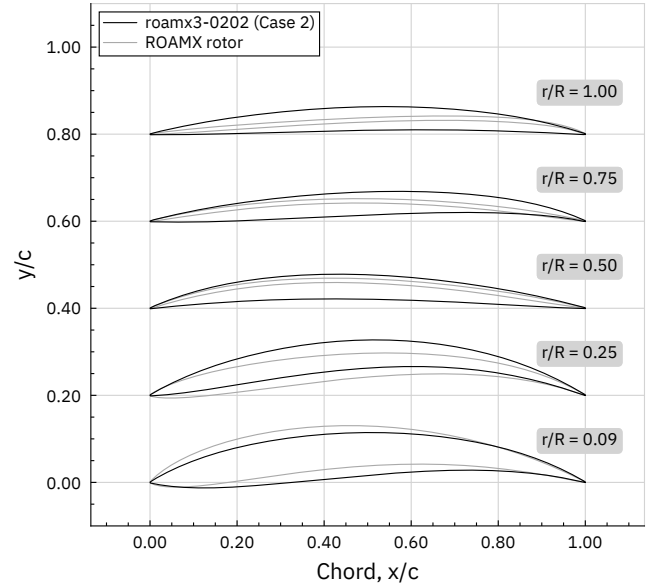


Figure 26. Example airfoil geometries for roamx3-0202 airfoil optimization at $C_T/\sigma = 0.175$, compared to the ROAMX rotor.

SAMPLE RECOVERY HELICOPTER COAXIAL ROTOR OPTIMIZATION

Recently, the Sample Recovery Helicopter (SRH) element was announced [42], serving as the primary backup for soil sample tube retrieval as part of the Mars Sample Return

(MSR) Campaign.[†] The MSR program aims to bring Mars materials back to Earth for the first time. Under current planning, a Sample Retrieval Lander (SRL) will bring a small rocket, the Mars Launch System (MLS) and two Sample Recovery Helicopters to Mars in 2030. The SRH mission leverages the design heritage of Ingenuity: each helicopter consists of an Ingenuity-like rotorcraft with the addition of ground mobility and a manipulator. An experimental validation campaign to explore higher thrust from an Ingenuity-like rotor was performed by the Jet Propulsion Laboratory (JPL) with support from AeroVironment, Inc. [24, 42]. The SRH mission element leverages the technical capabilities demonstrated by Ingenuity. The increased mass of the vehicle (due to the ground mobility and manipulator) requires increased rotor thrust and power, reducing control and power margins. The ELISA optimization toolset was used to optimize the Ingenuity coaxial rotor hover performance, while keeping the heritage airfoils [22] along the blade. Several thrust-weighted solidities of $\sigma = 0.135$, 0.150, 0.180 and 0.210 were investigated to identify possible performance improvements.

Rotor Optimization

As the airfoils are not optimized for this study, variation of angle of attack with azimuth is not a concern and the coaxial performance can be readily evaluated. Blade twist and planform were both parameterized using cubic Bézier curves. The Pareto-optimal rotor set for $\sigma = 0.135$ is shown in Figure 27.

Of the available solidities, the $\sigma = 0.150$ Pareto-optimal rotor set ultimately was studied in greater detail. Figure 28 shows the Pareto-optimal rotor set for Figure of Merit as function of blade loading.

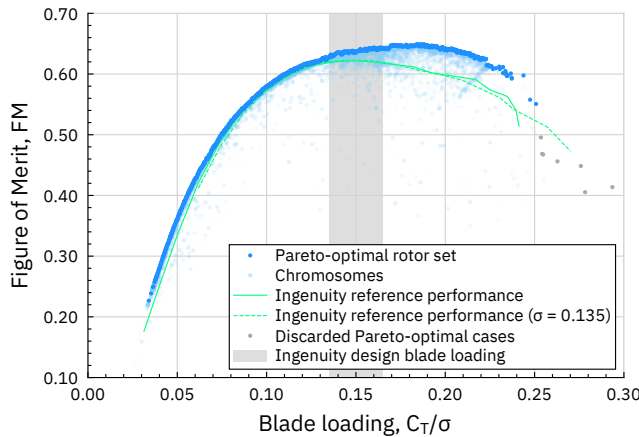


Figure 27. Coaxial optimization of planform and twist for $\sigma = 0.135$.

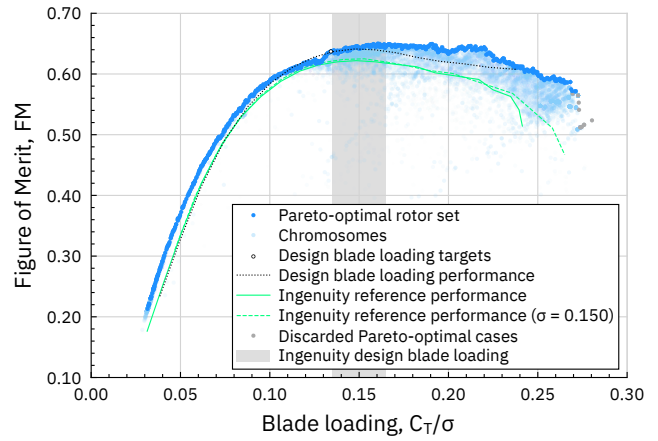


Figure 28. Coaxial optimization of planform and twist for $\sigma = 0.150$.

The optimization resulted in an SRH risk-reduction rotor design. Figure 29 shows the twist and chord distributions for this design condition and compares to the Ingenuity distributions. The outboard twist distribution is virtually unchanged from Ingenuity, but the chord distribution shows a different trend, most notably near tip. The blade geometry was analyzed for structural properties, manufacturability, and integration by AeroVironment, Inc., who also modified the root geometry to arrive at the ‘final’ risk-reduction blade twist and planform distributions.

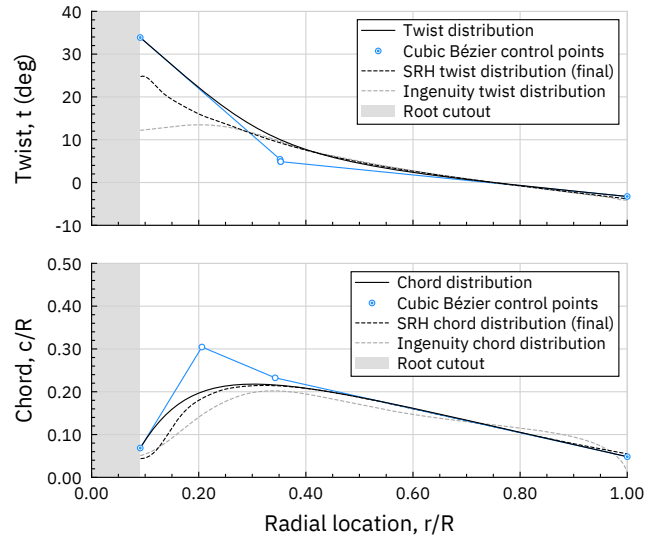


Figure 29. Sample Recovery Helicopter risk-reduction rotor planform and twist, compared to Ingenuity.

Optimizations were performed using identical upper and lower blades, as well as a separate optimization allowing for different upper and lower blades. No significant differences were observed for the latter approach, so in favor of the

[†] The decision to implement Mars Sample Return will not be finalized until NASA’s completion of the National Environmental Policy Act (NEPA) process. This document is being made available for information purposes only.

smaller design space, the identical blades were ultimately studied in more detail.

NEXT-GENERATION AIRFOIL OPTIMIZATION FOR COMPRESSIBLE LOW-REYNOLDS NUMBERS

Further studies into possible efficient airfoil shapes were performed using ELISA and various types of ROAMX parameterizations. Of particular significance was the roamx-1301 parameterization because of relatively high attainable lift-to-drag ratio figures. The operating conditions were chosen to reflect those at $r/R = 0.75$ as representative of the aerodynamics over the blade ($Re = 20,000$ and $M = 0.60$). The airfoil geometry obtained for peak c_l/c_d is presented in Figure 30.

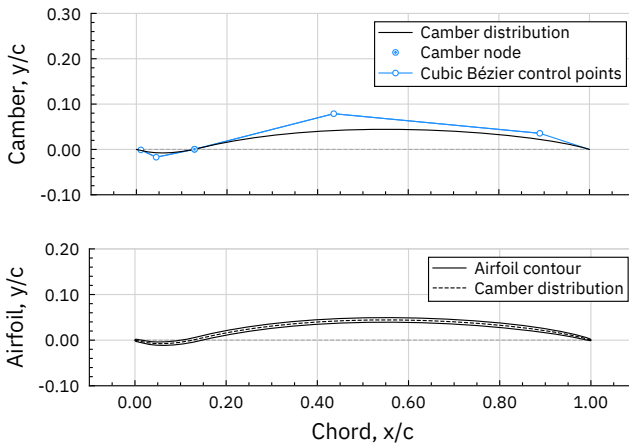


Figure 30. Peak c_l/c_d airfoil for roamx-1301 parameterization at $r/R = 0.75$.

The peak c_l/c_d for the airfoil optimizations at the tip are compared in Table 4 and the maximum relative change, compared to the clf5605 profile is around 42% at $r/R = 0.75$.

Table 4. Comparison of airfoil performance for $Re = 20,000$, $M = 0.60$.

Airfoil	c_l/c_d (peak)	Relative change, %	Section lift, c_l	Angle of attack, α
clf5605	19.90	--	0.91	2.50 ^d
roamx-0201	25.89	28%	1.13	4.48
roamx-1301	28.25	42%	1.02	3.61

^dResolution of $\alpha = 0.25$ degrees used to find peak lift-to-drag ratio.

Flow Physics

Figure 31 shows a schematic representation of the flow physics. Similar to the roamx-0201 based airfoils as shown in Figure 32, the sharp leading edge causes immediate separation of the boundary layer. The separated shear layer rapidly becomes unstable (a Kelvin-Helmholtz type

instability, in absence of any small scales) and starts shedding large scale vortices.

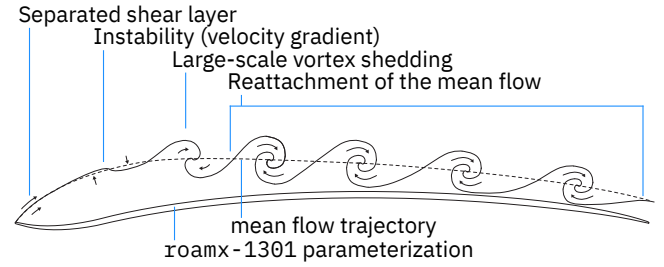


Figure 31. Schematic flow physics over optimized roamx-1301 parameterized airfoil.

The roamx-0201 optimal geometry optimizes to a higher angle of attack (as shown in Table 4), with a mean maximum Mach number of $M = 0.99$. The near sonic mean peak Mach number likely reveals the optimization tradeoff: the quadratic Bézier curve has to represent positive camber for efficient section performance, but it also introduces a geometric requirement that the angle of attack is sufficiently high to generate a separated shear layer with a strong velocity gradient to induce the instabilities. The angle of attack is, however, rapidly constrained by the (mean) maximum Mach number to avoid strong adverse effects from supersonic (mean) flow.

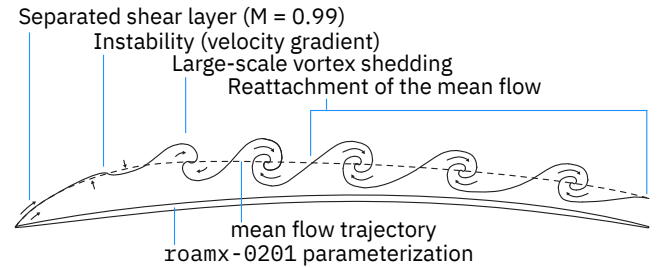


Figure 32. Schematic flow physics over optimized roamx-0201 parameterized airfoil.

In absence of rapid breakdown to turbulence, the reattachment process is an unsteady phenomenon with large spanwise structures shedding into the turbulent boundary layer. The ‘raised lip’ of the LE allows the separated shear layer to become unsteady and the aft part of the airfoil is aligned with the trajectory of the vortices. The instantaneous flowfield around the roamx-1301 airfoil at several timesteps is shown in Figure 33. For comparison the instantaneous flowfield around the roamx-0201 airfoil is shown in Figure 34.

The pressure distribution around the roamx-1301 airfoil is presented in Figure 35, showing both the instantaneous and mean pressure distributions, corresponding to the flowfields presented in Figure 31. The instantaneous result shows the suction peaks of the vortices as they convect downstream towards the TE for the time corresponding to Figure 33-B and Figure 33-C.

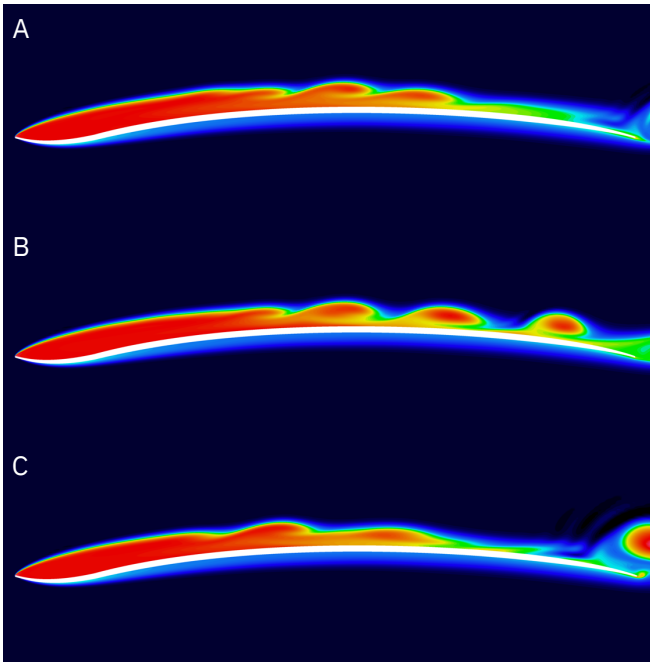


Figure 33. Instantaneous flow field around a roamx-1301 parameterized airfoil at several timesteps.

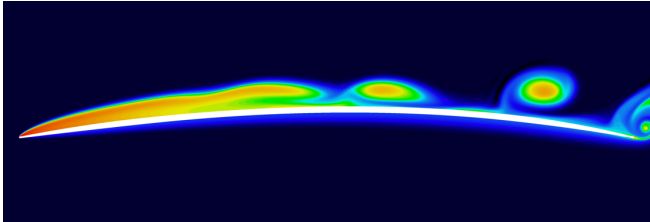


Figure 34. Instantaneous flow field around a roamx-0201 parameterized airfoil.

The mean flow presents a distribution akin to a reattached bubble that, in absence of any transition to small-scale turbulence, appears similar to flapping bubbles at higher Reynolds numbers [27]. The sharp leading edge will now, however, promote separation at a fixed location (i.e., the LE), in contrast to the usual sensitivity to operating conditions for conventional airfoils undergoing laminar separation.

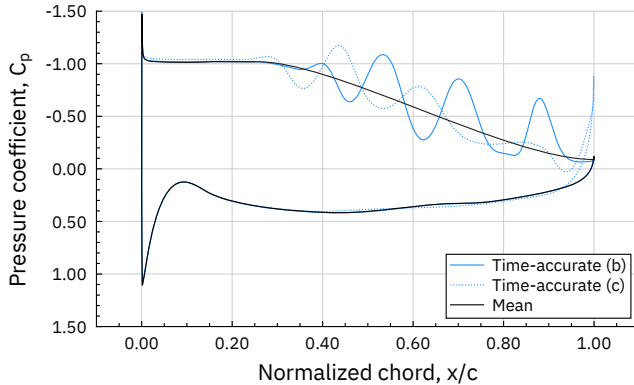


Figure 35. Pressure distribution around a roamx-1301 parameterized airfoil.

Sharp leading edges are key [25, 28-29] as they trigger shear layer separation at a fixed location (regardless of angle of attack and Reynolds number) and shear layer instabilities (large-scale vortex shedding). At higher Reynolds number, separation bubbles are generally omitted, if possible, since their existence always reduces performance compared to on-body transition of the boundary layer [27]. At very low Reynolds number, however, flapping bubbles can be beneficial, as in absence of transition to (small-scale) turbulence, they can help avoid full laminar separation.

Other section lift values for roamx-1301 airfoils resulted in a crest that is more directly aligned with the mean flow trajectory, as shown in Figure 36. Early results have also shown this lifting mechanism is applicable for thicker profiles.

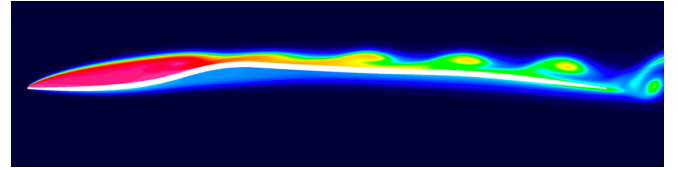


Figure 36. Instantaneous flow field around a roamx-1301 parameterized airfoil.

Rotor optimizations with this airfoil profile have been performed for the same conditions as the ROAMX rotor and reached a predicted $FM = 0.68$, the highest rotor hover efficiency found to date for these conditions. Practical considerations such as radial interpolation and manufacturability of the blade is still a topic of active research.

CONCLUDING REMARKS

The main conclusions for this work are presented here.

1. The Evolutionary aLgorithm for Iterative Studies of Aeromechanics (ELISA) was developed in support of the Rotorcraft Optimization for the Advancement of Mars eXploration (ROAMX) project.
2. The ELISA optimization toolset was described, introducing the ROAMX airfoil parameterization scheme, Pareto-optimal C81 deck (PO-C81) generation, post-airfoil optimization of the blade, and integration with rotating blade structural analyses.
3. Full optimization of the ROAMX rotor was presented and demonstrated possible increases in peak Figure of Merit of up to 19% over Ingenuity.
4. A coaxial rotor optimization was performed for Ingenuity's heritage airfoils, to modify the twist and planform to allow for increased performance. The optimization resulted in the Sample Recovery Helicopter (SRH) risk-reduction rotor design.

5. Airfoil optimization using a roamx-1301 parameterization resulted in airfoil lift-to-drag ratio increases of up to 42% over Ingenuity's clf5605 outboard airfoil for representative conditions at $r/R \approx 0.75$. Preliminary rotor optimization, constrained to Ingenuity rotor dimensions, predicted a Figure of Merit of 0.68 using these profiles outboard.

FUTURE WORK

Experimental testing has been performed at the Tohoku University Mars Wind Tunnel, Japan, for the clf5605 and roamx-0201 airfoil. The operating conditions were chosen to reflect those at $r/R = 0.75$ as representative of the aerodynamics over the blade ($Re = 20,000$ and $M = 0.60$). The experimental data will be used to further investigate the performance of these airfoils and compare to CFD analyses in OVERFLOW. Further collaboration is being set up with Imperial College London to allow their Direct Numerical Simulations (DNS) using PyFR [12-14] to complement the analyses and provide full insight into the aerodynamic behavior of these airfoils at compressible low Reynolds number conditions.

Early studies showed that relative sectional performance improvements are valid in 3D environments. More analysis will need to be performed to evaluate the airfoil performance in 3D environments, both for the airfoil performance (as an extruded 2D profile) as well as the impact of their usage on a practical rotor blade with spanwise variation of airfoils and planform. Similarly, the evaluation of potential shocks near the blade tip, and the implications of evaluation sectional performance versus true 3D environments deserves further attention.

ELISA has numerous possible efficiency improvements that can be studied and developed, including improvements in convergence by utilizing an Adaptive Genetic Algorithm that alters the Multi-Objective Genetic Algorithm (MOGA) hyperparameters (genetic operator probabilities, gene (per)mutation probabilities) as function of generation. Tuning of MOGA hyperparameters for the rotor optimization segment will be studied to improve convergence statistics.

Future work will also expand on airfoil optimization with Reynolds number as a third objective to investigate optimal shapes as function of Reynolds number and Mach number. This could result in a surrogate model that could replace the airfoil optimization altogether for a wide range of Reynolds numbers. MOGA is particularly well suited to generating surrogate model input – MOGA is effective in searching 3D space, compared to running a predefined matrix of cases.

Integration of structural analyses within the ELISA optimization toolset, instead of allowing for iterations of a structural metric, would improve the usefulness of the toolset. When a structural model is implemented within the loop,

varying alpha with azimuth, and therefore forward flight optimization, could become possible. Rotor optimization can be evaluated along a mass axis and elastic deformations can be fed back into the rotor optimization.

PARSEC airfoil parameterization is currently being implemented into the code to allow for efficient, strictly-conventional airfoil optimization. This, in combination with the significantly reduced computation time of airfoil performance at higher Reynolds numbers, could allow the ELISA optimization toolset to be used for higher Reynolds number analyses.

Further investigation of roamx-1301 like parameterizations, and their implementation in 3D blades, could lead to advancements in rotor performance at these conditions.

Author contact:

Witold J. F. Koning witold.koning@nasa.gov

B. Natalia Perez Perez natalia.perezperez@nasa.gov

Haley V. Cummings haley.cummings@nasa.gov

Ethan A. Romander ethan.romander@nasa.gov

Wayne Johnson wayne.johnson@nasa.gov

ACKNOWLEDGMENTS

Ravi Lumba, Cheng Chi, and Anubhav Datta are thanked for the helpful discussions and their invaluable support in completing this work. The research of Witold J. F. Koning, B. Natalia Perez Perez, and Haley Cummings is made possible by the NASA FY21 Space Technology Mission Directorate Early Career Initiative Project “Rotor Optimization for the Advancement of Mars eXploration.” Lidia Caros, Oliver Buxton, and Peter Vincent are thanked for helpful discussions and expertise. The authors would like to acknowledge the support of William Warmbrodt and Larry Hogle during this research. Tove Ågren, Nicholas Peters, and Sesi Kottapalli are thanked for their feedback in reviewing this paper. Resources supporting this work were provided by the NASA High-End Computing Program through the NASA Advanced Supercomputing Division at Ames Research Center.

REFERENCES

- [1] Balaram, J. (Bob), Canham, T., Duncan, C., Golombek, M., Grip, H. F., Johnson, W., Maki, J., Quon, A., Stern, R., and Zhu, D., “Mars Helicopter Technology Demonstrator,” AIAA Science and Technology Forum and Exposition (AIAA SciTech), AIAA Paper 2018- 0023, January 2018. <https://doi.org/10.2514/6.2018-0023>.
- [2] Escobar, D., Chopra, I., and Datta, A., “Aeromechanical Loads on a Mars Coaxial Rotor,” American Helicopter Society 74th Annual Forum and Technology Display, Phoenix, AZ, U.S.A., May 2018.

- [3] Escobar, D., Chopra, I., and Datta, A., "Aeromechanics of a Coaxial Mars Helicopter Using High-Fidelity CFD/CA," Vertical Flight Society's 75th Annual Forum & Technology Display, Philadelphia, PA, U.S.A., May 2019.
- [4] Lumba, R., Chi, C., Datta, A., Koning, W., Perez Perez, N., and Cummings, H., "Structural Design and Aeromechanical Analysis of Unconventional Blades for Future Mars Rotorcraft," *Journal of the American Helicopter Society*, 2023.
- [5] Chi, C., Lumba, R., Su Jung, Y., and Datta, A., "Aeromechanical Analysis of a Next-Generation Mars Hexacopter Rotor," *Journal of Aircraft*, Vol. 59, No. 6, 2022, pp. 1463–1477.
<https://doi.org/10.2514/1.C036739>
- [6] Anyoji, M., Ida, S., Nose, K., Numata, D., Nagai, H., and Asai, K., "Characteristics of the Mars Wind Tunnel at Tohoku University in CO₂ Operation Mode," 48th AIAA Aerospace Sciences, AIAA Paper 2010-1490, Orlando, FL, U.S.A., January 2010.
<https://doi.org/10.2514/6.2010-1490>
- [7] Anyoji, M., Nose, K., Ida, S., Numata, D., Nagai, H., and Asai, K., "Low Reynolds Number Airfoil Testing in a Mars Wind Tunnel," 40th Fluid Dynamics Conference and Exhibit, AIAA Paper 2010-4627, Chicago, IL, U.S.A., June-July 2010.
<https://doi.org/10.2514/6.2010-4627>
- [8] Munday, P. M., Taira, K., Suwa, T., Numata, D., and Asai, K., "Nonlinear Lift on a Triangular Airfoil in Low-Reynolds-Number Compressible Flow," *Journal of Aircraft*, Vol. 52, No. 3, 2014, pp. 924–931.
<https://doi.org/10.2514/1.C032983>
- [9] Anyoji, M., Nose, K., Ida, S., Numata, D., Nagai, H., and Asai, K., "Development of a Low-Density Wind Tunnel for Simulating Martian Atmospheric Flight," *Transactions of the Japan Society for Aeronautical and Space Sciences, Aerospace Technology Japan*, Vol. 9, 2011, pp. 21–27.
<https://doi.org/10.2322/tastj.9.21>
- [10] Nagata, T., Sato, H., Okochi, M., Matsuyama, T., Sugioka, Y., Kasai, M., Kusama, K., Numata, D., Nonomura, T., and Asai, K., "Visualization of Pressure and Skin-Friction Fields on Rotating Blade under Low-Pressure Conditions," *AIAA Journal*, Vol. 60, No. 9, 2022, pp. 5422–5435.
<https://doi.org/10.2514/1.J061638>
- [11] Guilarte Herrero, A., Noguchi, A., Kusama, K., Shigeta, T., Nagata, T., Nonomura, T., and Asai, K., "Effects of Compressibility and Reynolds Number on the Aerodynamics of a Simplified Corrugated Airfoil," *Experiments in Fluids*, Vol. 62, 2021, pp. 1–20.
<https://doi.org/10.1007/s00348-021-03164-0>
- [12] Caros, L., Blank, J., Buxton, O., and Vincent, P., "Comparing Strategies for DNS Based Optimization of Airfoils for Martian Rotorcraft," *Vertical Flight Society's 78th Annual Forum & Technology Display*, Fort Worth, TX, U.S.A., May 2022.
- [13] Caros, L., Buxton, O., Shigeta, T., Nagata, T., Nonomura, T., Asai, K., and Vincent, P., "Direct Numerical Simulation of Flow over a Triangular Airfoil Under Martian Conditions," *AIAA Journal*, Vol. 60, No. 7, 2022, pp. 3961–3972.
<https://doi.org/10.2514/1.J061454>
- [14] Caros, L., Buxton, O., and Vincent, P., "Optimization of Triangular Airfoils for Martian Helicopters Using Direct Numerical Simulations," *AIAA Journal*, Vol. 61, No. 11, 2023, pp. 4935–4945.
<https://doi.org/10.2514/1.J063164>
- [15] Desert, T., Moschetta, J.-M., and Bezard, H., "Numerical and Experimental Investigation of an Airfoil Design for a Martian Micro Rotorcraft," *International Journal of Micro Air Vehicles*, Vol. 10, No. 3, 2018, pp. 262–272.
<https://doi.org/10.1177/1756829318794171>
- [16] Désert, T., Jardin, T., Bézard, H., and Moschetta, J.-M., "Numerical Predictions of Low Reynolds Number Compressible Aerodynamics," *Aerospace Science and Technology*, Vol. 92, September 2019, pp. 211–223.
<https://doi.org/10.1016/j.ast.2019.05.064>
- [17] Carreno Ruiz, M., and D'Ambrosio, D., "Hybrid Fidelity Optimization of Efficient Airfoils and Rotors in Ultra-Low Reynolds Numbers Conditions," AIAA Science and Technology Forum and Exposition (AIAA SciTech), AIAA Paper 2023-0652, National Harbor, MD, U.S.A., January 2023.
<https://doi.org/10.2514/6.2023-0652>
- [18] Carreno Ruiz, M., and D'Ambrosio, D., "ROT8: A Matlab App for Low Reynolds Number Airfoil and Rotor Aerodynamic Design," AIAA AVIATION 2023 Forum, AIAA Paper 2023-3379.c1, San Diego, CA, U.S.A., June 2023.
<https://doi.org/10.2514/6.2023-3379.c1>
- [19] Yoshikawa, K., Buto, Y., Sato, M., Oyama, A., Sugiura, M., Tanabe, Y., Kimura, K., Takekawa, K., Kishi, Y., and Kanazaki, M., "Compressibility Effects on Aerodynamic Characteristics and Flow Fields of Mars Helicopter Rotor," AIAA AVIATION 2023 Forum, AIAA Paper 2023-4000, San Diego, CA, U.S.A., June 2023.
<https://doi.org/10.2514/6.2023-4000>
- [20] Kishi, Y., Kanazaki, M., Sugiura, M., Tanabe, Y., Oyama, A., and Sato, M., "Numerical Analysis on Hovering Performance of Hexacopter 'HAMILTON' for Mars Exploration," AIAA AVIATION 2022 Forum, AIAA Paper 2022-4039, Chicago, IL, U.S.A., June-July 2022.
<https://doi.org/10.2514/6.2022-4039>
- [21] Yamaguchi, T., and Anyoji, M., "Numerical Study on Low-Reynolds Compressible Flows around Mars Helicopter Rotor Blade Airfoil," *Journal of Flow Control, Measurement & Visualization*, Vol. 11, No. 2, April 2023, pp. 30–48.
10.4236/jfcmv.2023.112003

- [22] Koning, W. J. F., Johnson, W., and Allan, B. G. "Generation of Mars Helicopter Rotor Model for Comprehensive Analyses" American Helicopter Society Technical Conference on Aeromechanics Designs for Transformative Vertical Flight, San Francisco, CA, January 2018.
- [23] Koning, W. J. F., Johnson, W., and Grip, H. F., "Improved Mars Helicopter Aerodynamic Rotor Model for Comprehensive Analyses," *AIAA Journal*, Vol. 57, No. 9, September 2019.
<https://doi.org/10.2514/1.J058045>
- [24] Koning, W. J. F., Allan, B. G., Romander, E. A., and Johnson, W., "Comparing 3D and 2D CFD for Mars Helicopter Ingenuity Rotor Performance Prediction," 49th European Rotorcraft Forum, Bückeburg, Germany, September 2023.
- [25] Koning, W. J. F., Romander, E. A., and Johnson, W., "Low Reynolds Number Airfoil Evaluation for the Mars Helicopter Rotor," *AHS International 74th Annual Forum & Technology Display*, Phoenix, AZ, U.S.A., May 2018.
- [26] Argus, F. J., Ament, G. A., and Koning, W. J. F., "The Influence of Laminar-Turbulent Transition on Rotor Performance at Low Reynolds Numbers," VFS Aeromechanics for Advanced Vertical Flight Technical Meeting, San Jose, CA, U.S.A., January 2020.
- [27] Koning, W. J. F., Romander, E. A., Cummings, H. V., Perez, B. N., and Buning, P. G. "On Improved Understanding of Airfoil Performance Evaluation Methods at Low Reynolds Numbers." *Journal of Aircraft*, Vol. 60, No. 3, May 2023.
<https://doi.org/10.2514/1.C037023>
- [28] Koning, W. J. F., Romander, E. A., and Johnson, W., "Optimization of Low Reynolds Number Airfoils for Martian Rotor Applications Using an Evolutionary Algorithm," AIAA Science and Technology Forum and Exposition (AIAA SciTech), AIAA Paper 2020-0084, 2020, Orlando, FL, U.S.A., January 2020.
<https://doi.org/https://doi.org/10.2514/6.2020-0084>
- [29] Koning, W. J. F., Romander, E. A., and Johnson, W., "Performance Optimization of Plate Airfoils for Martian Rotor Applications Using a Genetic Algorithm," 45th European Rotorcraft Forum, Warsaw, Poland, September 2019.
- [30] Johnson, W., Withrow-Maser, S., Young, L., Malpica, C., Koning, W. J. F., Kaung, W., Fehler, M., Tuano, A., Chan, A., Datta, A., Chi, C., Lumba, R., Escobar, D., Balaram, J., Tzanetos, T., and Grip, H. F., "Mars Science Helicopter Conceptual Design," Moffett Field, CA, U.S.A., NASA/TM-2020-220485, 2020.
- [31] Cummings, H., Perez, B. N. P., Koning, W., Johnson, W., Young, L., Haddad, F., Romander, E., Balaram, J., Tzanetos, T., and Bowman, J., "Overview and Introduction of the Rotor Optimization for the Advancement of Mars eXploration (ROAMX) Project," VFS Aeromechanics for Advanced Vertical Flight Technical Meeting, San Jose, CA, U.S.A., January 2022.
- [32] Holst, T. L., and Pulliam, T. H., "Evaluation of Genetic Algorithm Concepts Using Model Problems. Part 1; Single-Objective Optimization," Moffett Field, CA, U.S.A., NASA, 2003.
- [33] Holst, T. L., and Pulliam, T. H., "Evaluation of Genetic Algorithm Concepts Using Model Problems. Part 2; Multi-Objective Optimization," Moffett Field, CA, U.S.A., NASA/TM-2003-212813/PT2, 2003.
- [34] Pulliam, T., Nemec, M., Holst, T., and Zingg, D., "Comparison of Evolutionary (Genetic) Algorithm and Adjoint Methods for Multi-Objective Viscous Airfoil Optimizations," 41st Aerospace Sciences Meeting and Exhibit, Reno, NV, U.S.A., January 2003.
<https://doi.org/10.2514/6.2003-298>
- [35] Nichols, R. H., and Buning, P. G. "User's Manual for OVERFLOW 2.2." Langley Research Center, Hampton, VA, 2008
- [36] Pulliam, T. H., "High Order Accurate Finite-Difference Methods: As Seen in OVERFLOW." 20th AIAA Computational Fluid Dynamics Conference, AIAA Paper 2011-3851, Honolulu, HI, U.S.A., June 2011.
- [37] Tramel, R., Nichols, R., and Buning, P., "Addition of Improved Shock-Capturing Schemes to OVERFLOW 2.1." 19th AIAA Computational Fluid Dynamics, AIAA Paper 2009-3988, San Antonio, TX, U.S.A., June 2009.
<https://doi.org/doi:10.2514/6.2009-3988>
- [38] Pulliam, T. H. "Time Accuracy and the Use of Implicit Methods." 11th AIAA Computational Fluid Dynamics Conference, AIAA Paper 1993-3360, Orlando, FL, U.S.A., July 1993.
<https://doi.org/10.2514/6.1993-3360>.
- [39] Pandya, S., Venkateswaran, S., and Pulliam, T. H. "Implementation of Preconditioned Dual-Time Procedures in OVERFLOW." AIAA 41st Aerospace Sciences Meeting, AIAA Paper 2003-0072, Reno, NV, U.S.A., Jan. 2003.
<https://doi.org/10.2514/6.2003-72>.
- [40] Bergmann, M., Morsbach, C., Ashcroft, G., and Kügeler, E., "Statistical Error Estimation Methods for Engineering-Relevant Quantities from Scale-Resolving Simulations," *Journal of Turbomachinery*, Vol. 144, No. 3, 2022.
<https://doi.org/10.1115/1.4052402>

- [41] Johnson, W. "Rotorcraft Aerodynamics Models for a Comprehensive Analysis." AHS International 54th Annual Forum & Technology Display, Fairfax, VA, U.S.A., 1998.
- [42] Mier-Hicks, F., Grip, H. F., Kalantari, A., Moreland, S., Pipenberg, B., Keennon, M., Canham, T. K., Pauken, M., Decrossas, E., and Tzanetos, T. "Sample Recovery Helicopter." 2023 IEEE Aerospace Conference, Big Sky, MT, U.S.A., 2023.
doi: 10.1109/AERO55745.2023.10115951.